



Nanoscale

TiO₂ superstructures with oriented nanospaces: A strategy for efficient and selective photocatalysis

Journal:	<i>Nanoscale</i>
Manuscript ID	NR-ART-12-2019-010435.R1
Article Type:	Paper
Date Submitted by the Author:	04-Feb-2020
Complete List of Authors:	Murakami, Yuta; Kobe University, Department of Chemistry, Graduate School of Science Kamegawa, Takashi; Osaka Prefecture University, Department of Applied Chemistry, Graduate School of Engineering Kobori, Yasuhiro; Kobe University, Molecular Photoscience Research Center Tachikawa, Takashi; Kobe University, Molecular Photoscience Research Center

SCHOLARONE™
Manuscripts

ARTICLE

TiO₂ superstructures with oriented nanospaces: A strategy for efficient and selective photocatalysis

Yuta Murakami,^a Takashi Kamegawa,^b Yasuhiro Kobori^{ac} and Takashi Tachikawa^{*ac}Received 00th January 20xx,
Accepted 00th January 20xx

DOI: 10.1039/x0xx00000x

Highly ordered superstructures of semiconductor nanocrystals contain abundant nanometer-scale pores between the crystals; however, there have been difficulties in controlling the size and orientation of these nanospaces without the use of a template or a capping reagent. This constraint has affected their development and applications in potential fields including catalysis and optoelectronics adversely. In this study, we synthesized a rod-shaped TiO₂ mesocrystal (TMC) having a length of a few hundreds of micrometers and comprising regularly ordered anatase TiO₂ nanocrystals that form oriented nanospaces by exposed {001} facets. Finite-difference time-domain (FDTD) calculations of electric fields and in situ fluorescence imaging with a polarization sensitive dye on a single mesocrystal were performed to reveal anisotropic adsorption and excitation of the dyes. Furthermore, the photodegradation of the dyes was found to be more facilitated in nanospaces formed by the specific facets, as compared with the dyes randomly adsorbed on the outer surfaces. Consequently, enhancing the selectivity of photocatalytic reactions on molecular size and redox was achieved by introducing the concept of oriented nanospace.

1. Introduction

Nanoporous metal oxide materials have received growing attention in many fields, especially energy conversion, energy storage, and drug delivery, owing to their unique adsorptive and catalytic properties.¹⁻⁴ Soft chemistry, which is a type of chemistry to prepare final materials from molecular precursors at low temperatures and pressures, is a well-established means to synthesize mesoporous structures using surfactants, block copolymers, or colloids as sacrificial templates.^{5,6} Metal-organic frameworks (MOFs) have recently emerged as alternative templates to produce inorganic architectures with nanoscale periodicity, owing to their structural diversity and designability.^{7,8} However, the applications of nanoporous metal oxides in photocatalysis and photovoltaics still remain limited despite their impressive characteristics, because of their complex synthesis procedures, mechanical instability, and poor electronic conductivity.

TiO₂ has been recognized as an important semiconductor material in applications such as photodegradation of pollutants, water splitting, dye-sensitized solar cells, and lithium-ion batteries.⁹⁻¹⁵ Recently, it has been verified that TiO₂ mesocrystals (TMCs), which are assemblies of crystallographically oriented TiO₂ nanocrystals, promote spatial separation of photogenerated

charge carriers, and they are often more efficient than nanoparticle systems in photocatalytic reactions such as dye degradation and hydrogen evolution.¹⁶⁻¹⁹ The alignment of nanocrystals is a critical factor for efficient charge carrier separation in mesocrystals.²⁰⁻²³ Besides the TiO₂ mesocrystals, there are binary metal oxide mesocrystals (e.g., ZnO/CuO mesocrystals) and quantum dot systems (e.g., superlattices) that cause efficient charge transfer and energy transfer, respectively, by controlling the space between particles.²⁴⁻²⁷

Photocatalytic activity of metal oxides is highly dependent on the exposed crystal facets in addition to their specific surface area, composition, and crystal size.²⁸⁻³¹ The crystal-face dependences of adsorption affinity and reactivity have been studied on TiO₂ nanocrystals, microcrystals, and mesocrystals systematically by changing the ratio of the exposed crystal facets.³²⁻³⁵ It is nowadays widely accepted that the {001} and {101} facets of anatase TiO₂ are more favorable for oxidation and reduction reactions, respectively.^{36,37} Selective photoreduction by suppressing the oxidation counterpart is extremely important (or vice versa),³⁸ for example, for making NO_x harmless during photocatalytic reactions,³⁹ and such selective reactions generally require the presence of hole (h⁺) or electron (e⁻) scavengers to avoid charge recombinations.^{40,41}

In spite of the crystal-face-dependent properties, much less attention has been devoted to the nanometer-scale pores formed by specific crystal faces in alignment with their crystallographic axes.⁴²⁻⁴⁴ For example, it has been suggested that oriented attachment (OA) of nanocrystals produces such nanospaces and induces periodic and anisotropic electrostatic fields between the particles, as predicted by molecular dynamics simulations.^{45,46} Although the OA has been proven to be a promising approach,⁴⁷ there is little clarity on the fabrication of three-dimensional

^a Department of Chemistry, Graduate School of Science, Kobe University, 1-1 Rokkodai-cho, Nada-ku, Kobe 657-8501, Japan

^b Department of Applied Chemistry, Graduate School of Engineering, Osaka Prefecture University, 1-2, Gakuen-cho, Naka-ku, Sakai, Osaka 599-8570, Japan

^c Molecular Photoscience Research Center, Kobe University, 1-1 Rokkodai-cho, Nada-ku, Kobe 657-8501, Japan

† Electronic Supplementary Information (ESI) available. See DOI: 10.1039/x0xx00000x

architectures of nanocrystals with a high degree of crystallographic alignment. Well-designed nanospaces would facilitate screening of target molecules by controlling the space sizes and their environment polarities in photocatalysis.⁴⁸⁻⁵⁰

In this study, we developed a novel concept called oriented nanospaces that are formed by a controlled alignment of well-faceted nanocrystals to realize selective photocatalysis by spatially separating the active sites for the reduction and oxidation. For this purpose, we newly synthesized rod-like TMCs by topotactic transformation from $(\text{NH}_4)_2\text{TiOF}_4$ -based precursor crystals. Since the synthesized TMC has an anisotropic shape, it is possible to readily associate the macroscopic morphology with the orientation of nanocrystals, and it is thus suitable for investigating the impact of oriented nanospaces by specific crystal facets. With the aid of theoretical calculations that predict local electric fields in the spaces, in situ fluorescence imaging on a single mesocrystal revealed that photodegradation of adsorbed dyes occurred in the oriented nanospaces by the $\{001\}$ facets better than those on the surface exposed to surrounding environment. Moreover, the pore apertures of TMC suppress the access of substrates to (or the escape of products from) the interiors of the mesocrystals effectively, resulting in suppressed oxidation and enhanced reduction of certain substrates. These unique properties of the oriented nanospaces developed in this study provide a general guidance for the design of new photocatalyst and photovoltaic materials.

2. Experimental section

2.1 Preparation of TMC

A precursor solution consisting of TiF_4 (Aldrich), Milli-Q water, NH_4NO_3 (Wako), and NH_4F (Wako) (molar ratio = 1:117:6.6:4) was prepared based on a previous report.¹⁶ The solution was heated in a glass beaker at 85 °C for 10 h. It is necessary to cover the glass beaker with an aluminum foil having a single hole of ~0.1 mm diameter to prevent the solution from drying up during heating. The synthesized precursor crystals were collected with a spatula and then washed several times with Milli-Q water in a filtration. The powders were then calcinated in air using a heating rate of 10 °C min^{-1} at 400 or 800 °C for 2 h for fluorescence microscopy measurements.

2.2 Characterization of materials.

The crystal structures of the samples were characterized using a powder X-ray diffractometer (XRD) (Smartlab, Rigaku; $\text{Cu K}\alpha$ source) and a transmission electronic microscope (TEM) (JEM-2100F, JEOL; operated at 200 kV). The morphologies were investigated using a scanning electron microscope (JSM-5500, JEOL) and a field-emission scanning electron microscope (FE-SEM) (SU8010, Hitachi). The Brunauer-Emmett-Teller (BET) surface areas were measured using a nitrogen sorption instrument (BEL-SORP mini; BEL Japan). The steady-state UV-vis absorption, diffuse reflectance, and fluorescence spectra were measured using a UV-vis spectrophotometer (V-770, JASCO) and a fluorescence spectrophotometer (FP-8300, JASCO). The

X-ray photoelectron spectroscopy (XPS) measurements were performed with the PHI X-tool (ULVAC-PHI).

2.3 Finite-difference time-domain (FDTD) calculations

The electric field distribution was calculated using a commercially available program (FDTD Solutions, Lumerical Inc). For these calculations, the refractive indices of the materials at excitation wavelengths were used as values in the software. The background refractive index was set to 1.0 (air). The simulation domain was set to 32 nm (x) \times 12.5 nm (y) \times 1400 nm (z) and was terminated with periodic boundary conditions in the transverse (x - y) plane and perfectly matched layer (PML) in the z direction. The mesh size was fixed at 0.125 nm.

2.4 Fluorescence microscopy measurements

The experimental setup was based on a Nikon Ti-E inverted wide-field fluorescence microscope. The 405 nm CW laser (Coherent, OBIS 405LX) through an objective lens (CFI Plan Apo λ 100 \times H, Nikon; NA 1.45) was used to excite 4-[4-(dimethylamino)styryl]pyridine (DMASP) in epi-illumination geometry, and the linearly polarized light through a half-wave plate (WPMH05M-405, Thorlabs) in indexed rotation mount was irradiated to TMC in each direction. The emission images were recorded on an electron-multiplying charge-coupled device (EMCCD) camera (Evolve 512, Roper Scientific) using the open source microscopy software Micro manager (<https://www.micro-manager.org/>). A suitable dichroic mirror (Di02-R405, Semrock) and a longpass filter (BLP01-458R, Semrock) were used to improve the signal-to-noise ratio. For the spectroscopy, only the emission that passed through a slit entered the imaging spectrograph (MS3504i, SOL instruments) equipped with a CCD camera (DU416A-LDC-DD, Andor). The data were analyzed using the open source image software ImageJ (<http://rsb.info.nih.gov/ij/>) and Origin 2019 (OriginLab). All experimental data were obtained at room temperature.

2.5 Photocatalytic activity tests

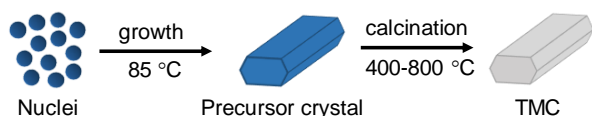
Rhodamine B (RhB) and 4-chlorophenol (4-CP) were used as target molecules. A TiO_2 dispersion (0.2 g L^{-1}) of 10 mL containing an aqueous solution ($[\text{RhB}] = 1.0 \times 10^{-5}$ M in neutral water; $[\text{4-CP}] = 1.5 \times 10^{-4}$ M in neutral water; and $[\text{Cr}^{6+}] = 4.0 \times 10^{-4}$ M in H_2SO_4 aqueous solution with a pH of 3) was prepared in a glass container. Prior to the photoirradiation, the substrate was adsorbed to TMC (sintered at 500 °C in oxygen atmosphere for 8 h to almost completely remove fluorine from the surface for photocatalytic activity tests (Fig. S1†)¹⁶, crushed TMC, and P25 until the adsorption equilibrium was reached. The photocatalytic reaction was initiated by a light-emitting diode (LED) (M365LP-1, Thorlabs) at room temperature. The intensity of the UV light was measured to be ca. 30 mWcm^{-2} . Subsequent to UV illumination, the sample was centrifuged at 10000 rpm (Model 3520, KUBOTA) to remove the particles. The concentration of unreacted molecules was analyzed using a UV-vis spectrophotometer at the characteristic wavelength, from which the degradation yield was calculated. To estimate the amount of adsorbed RhB molecules, the sample solutions containing the TMC powder were kept in the dark until the

adsorption equilibrium was reached, and the particles in solution were then completely removed by the centrifugation. The concentrations of the adsorbates were determined from the absorbance observed by UV-vis absorption experiments.

3. Results and discussion

3.1 Synthesis and structural characteristics of TMC

As illustrated in Fig. 1, rod-like $(\text{NH}_4)_2\text{TiOF}_4$ -based precursor crystals were obtained after heating a solution containing TiF_4 , NH_4F , and NH_4NO_3 in a glass beaker at 85°C . The length of the synthesized $(\text{NH}_4)_2\text{TiOF}_4$ -based rods was up to $\sim 700\ \mu\text{m}$ in a typical synthesis and can be reduced to $\sim 200\ \mu\text{m}$ on average by placing a piece of silicon wafer ($\sim 5\ \text{mm}^2$) into the solution in the beaker (Fig. S2†). This is because more seed crystals are formed on the silicon wafer.⁵¹ By sintering the rod-like precursor crystals at $400\text{--}800^\circ\text{C}$, they are topotactically transformed to TMCs via NH_4TiOF_3 , as confirmed by powder X-ray diffraction (XRD) (Fig. S3†), while their morphology is maintained.^{52,53} Along with the removal of large amounts of nitrogen and fluorine during heating, the mesocrystal structure forms micro- and mesopores



between self-assembled nanocrystals.

Fig. 1 Synthesis of TMC via topotactic transformation from a precursor crystal. By heating the solution at 85°C , nucleation and nuclear growth occur, and a rod-like $(\text{NH}_4)_2\text{TiOF}_4$ -based precursor crystal is formed. The topotactic transformation of the precursor crystal to TMC is performed at higher annealing temperatures ($400\text{--}800^\circ\text{C}$).

The peak positions of powder XRD patterns (Fig. 2a) of the TMCs sintered at 400°C (referred to as TMC-400) and 800°C (referred to as TMC-800) were identified as anatase TiO_2 . Using the Scherrer's equation, the mean crystallite sizes of the nanocrystals in TMC-400 and TMC-800 were estimated to be ~ 20 and ~ 30 nm, respectively (Fig. S4†). The size of the as-synthesized TMCs ranged from a few tens to several hundreds of micrometers, as observed by field-emission scanning electron microscopy (FE-SEM) (Fig. 2b). The size of the nanocrystals is also determined as several tens of nanometers, which is consistent with the XRD results (Fig. 2c). The annealing at 800°C results in the increase of particle and pore sizes, leading to relatively disordered structures (Fig. 2d). The characteristics of porous structures such as specific surface area, measured by N_2 adsorption-desorption measurements, are presented in the ESI (Fig. S5† and Table S1†).

The assembled structure of nanocrystals is also confirmed by TEM (Fig. 3a). Notably, a selected-area electron diffraction (SAED) pattern recorded for the assembly showed well-defined diffraction spots corresponding to the $[010]$ zone axis of single-crystal anatase TiO_2 (inset of Fig. 3a) as evidence of a mesocrystal structure.⁵⁴ An anatase TiO_2 structure synthesized using a solution containing fluoride ions is a truncated tetragonal bipyramid in which two $\{001\}$ facets are dominantly exposed with eight $\{101\}$ facets.⁵⁵ As seen from Fig. 3b, the distances

between the adjacent lattice fringes are $0.35\ \text{nm}$ and $0.24\ \text{nm}$, which are corresponding to the $\{101\}$ and $\{001\}$ facets, respectively. Thus, as modeled in Fig. 3c, the nanospaces are formed by the $\{001\}$ facets of neighboring nanocrystals and are oriented along the long axis of TMC, whereas the mesopores with wider size distribution are mainly formed by the $\{101\}$ facets that are also exposed to the surrounding environment. It is conceivable that the orientation of the TiO_2 nanocrystals is almost perfectly aligned within $\pm 5^\circ$, considering that the TMC was obtained by topotactic transformation of a single crystal precursor (Fig. S6a,b†). Since the surface energies of the crystal planes follow the order of $0.9\ \text{Jm}^{-2}$ for $(001) > 0.44\ \text{Jm}^{-2}$ for (101) ,⁵⁶ the $\{001\}$ facets are likely to be stacked on top of each other to form a thermodynamically stable structure. The TEM observations further revealed that the distance between two opposed $\{001\}$ facets, i.e., the size of nanospace, is $1.5 \pm 0.5\ \text{nm}$, which is smaller than the typical size of a mesopore ($2\text{--}50\ \text{nm}$) and close to the molecular scale (Fig. S6c-e†).

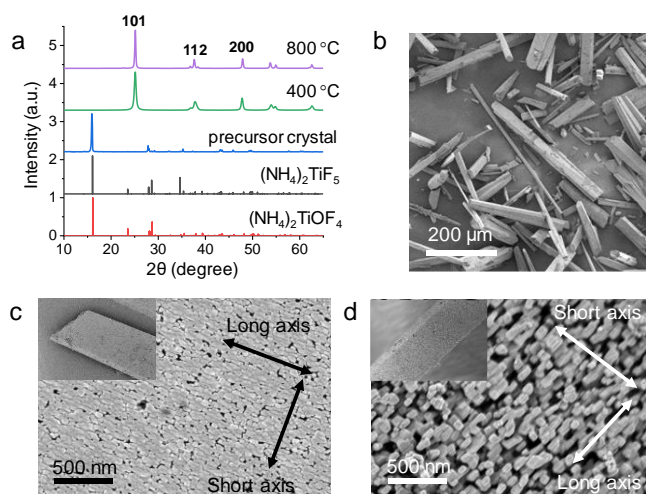


Fig. 2 (a) Powder XRD patterns of the samples. (b) FE-SEM image of TMC-400. FE-SEM images of crystal surfaces of (c) TMC-400 and (d) TMC-800. Insets show the low-magnification images of the measured samples.

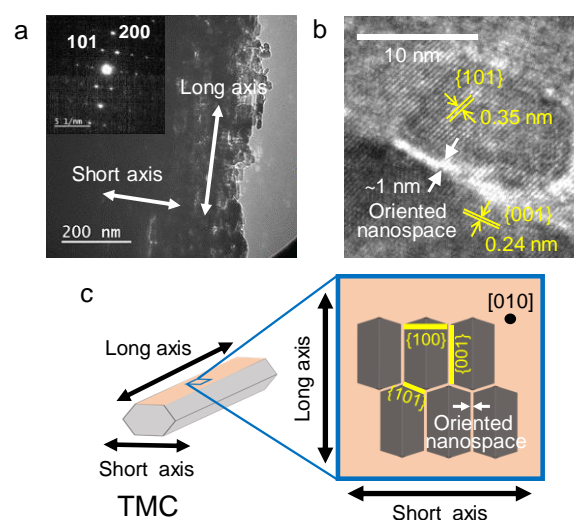


Fig. 3 (a) TEM image of TMC-400 showing an assembly of nanocrystals. Inset indicates the SAED pattern showing a single-crystal-like diffraction. (b) High-magnification TEM image of TMC-400. (c) Orientation of TiO_2 nanocrystals to the morphology of TMC. The

{101} facets are exposed on the surface of mesocrystal, and the {001} facets are arranged so as to create the oriented nanopores along the long axis of TMC.

3.2 FDTD calculations of electric field distributions

Prior to the fluorescence imaging experiments, we examined the distribution of electric fields based on finite difference time domain (FDTD) calculations. FDTD is a computational technique used to model electromagnetic fields.⁵⁷ For example, using this method, it was found that the TiO₂ porous layer gives many hot spots with significantly high electric fields.⁵⁸ This electric field enhancement effect of the nanostructured TiO₂ enables surface-enhanced Raman spectroscopic (SERS) detection of adsorbed molecules.⁵⁹

Fig. 4a shows a part of the structure used for the calculations (Fig. S7†). To model the TMC on the cover glass, eighteen rectangular TiO₂ particles with dimension of 16 nm (*x*) × 11 nm (*y*) × 16 nm (*z*) are assembled with a gap of 1.5 nm. The assembly is separated 4 nm from a SiO₂ substrate, because the actual TiO₂ particles are truncated tetragonal bipyramids (Fig. 3c). The electric field distributions calculated under different conditions are demonstrated in Fig. 4b-e. When 405-nm light polarized along the *y* axis is irradiated to the sample, a highly enhanced field is generated inside the nanopore (see panel b,d). Here, the enhancement factor (EF) is defined as $(|E|^2/|E_0|^2)$, where *E* and *E*₀ are local and incident electric fields, respectively. The maximum EF decreased from ca. 4.2 to ca. 2.9 when the gap is increased from 1.5 nm to 10 nm under the same excitation condition, indicating a significant role of the interplanar distance in the field enhancement (Fig. S8†). Meanwhile, when incident light is polarized along the *x* axis, only edges of the oriented nanopore exhibit the enhanced field (see panel c). Similar tendencies were observed when 365-nm light was irradiated (Fig. S9,S10†). It should be noted that light propagation into the TiO₂ particles is also affected by polarization of incident light.

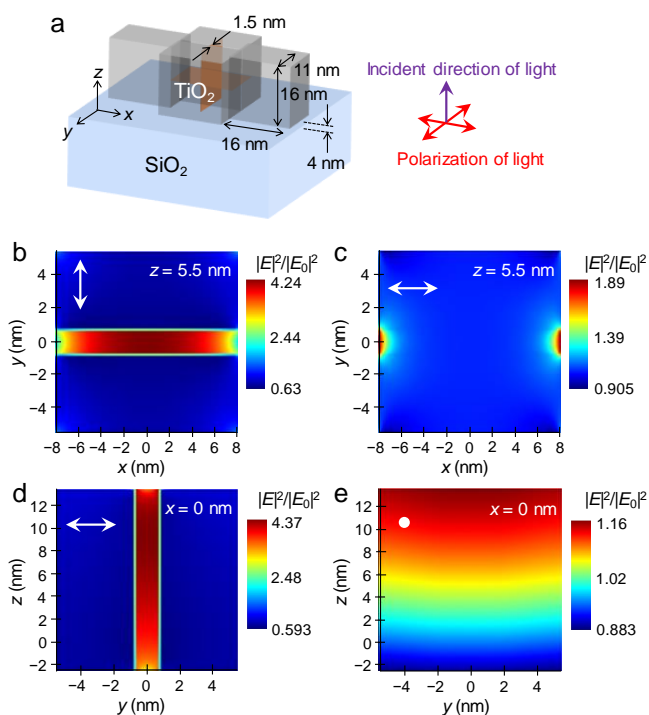
TiO₂ is more efficiently excited with *x*-axis polarized light, although local fields are slightly weakened near the pore entrance (*z* = -2.5 nm) (see panel e).

Fig. 4 (a) Structure used for the FDTD calculation. The purple and red arrows represent the incident direction of light ($\lambda = 405$ nm) and its polarization directions, respectively. (b,c) Distributions of electric fields obtained from the FDTD calculations in the gap of 1.5 nm between two rectangular TiO₂ particles at the *x*-*y* plane cut at the center of TiO₂ particle (*z* = 5.5 nm) when the polarization of the incident light is along *y* (b) and *x* (c) axes. (d,e) Distributions of electric fields at the *y*-*z* plane cut at the center of TiO₂ particle (*x* = 0 nm) when the polarization of the incident light is along *y* (d) and *x* (e) axes. See the orange planes in panel a for calculated regions. The arrows in panel b-e represent the polarization direction of incident light.

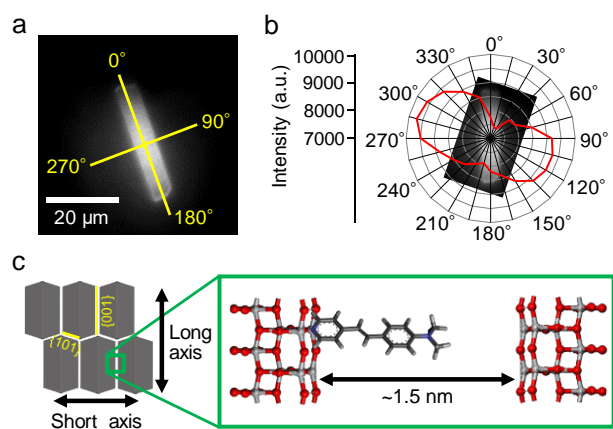
3.3 Fluorescence imaging of anisotropic dye adsorption and reaction

A fluorescence dye with polarization characteristics, DMASP,^{60,61} was used to explore the molecular adsorption and photocatalytic reaction in the oriented nanopores. The DMASP molecule can emit fluorescence only when the polarization of the excitation light is parallel to its transition dipole moment aligned with the long axis of the molecule (Fig. S11†). A small amount of TMC powder was added to a saturated solution of DMASP in acetonitrile, followed by washing with acetonitrile to remove excess molecules from the TMC surface. The resultant DMASP-adsorbed TMC exhibited a broad fluorescence spectrum with a wavelength maximum at ~575 nm, which is similar to that of a singly protonated form of DMASP in water, suggesting that the DMASP molecules bind to the Ti sites via the pyridine moiety (Fig. S12†).⁶¹ N 1s XPS measurements were performed to confirm the change in the electronic state upon adsorption of DMASP onto TMC (Fig. S13†). The peak position shifts by ~2 eV to the higher binding energy than that of an amorphous solid of DMASP, again suggesting a strong interaction between the electron-donating pyridine moiety of DMASP and TMC.⁶²

An acetonitrile suspension of DMASP-adsorbed TMC powder was then spin-coated on a clean cover glass for fluorescence imaging. By rotating a half-wave plate placed in front of the laser, the polarization of the excitation light to a single TMC was changed and the emission intensity was monitored with respect to the direction of each polarization (Fig. S14†). Fig. 5a shows the fluorescence image observed for a representative DMASP-adsorbed TMC-400 in ambient air under 405-nm laser excitation. The distribution of the fluorescence intensity in the image is due to a Gaussian profile of the excitation light intensity on the surface of the cover glass in a circle area with the diameter of ~40 μm. To verify the anisotropic adsorption, the fluorescence intensity as a response to the polarization of excitation light was examined. The polarization of the excitation light parallel to the long axis of TMC is defined as 0°. The laser intensity was carefully adjusted as constant as possible to ensure that even a slight change in anisotropy was detected. At the same time, it was also adjusted to be as weak as possible to ensure that the photobleaching of DMASP during measurements was suppressed. As demonstrated in Fig. 5b, there is an angle at which the intensity reaches its maximum value with a percentage difference (see Table 1 for definition) of about 20%; this suggests the presence of DMASP preferentially adsorbed on the



surface at a certain angle on average. The direction approximately parallel to the short axis of TMC is consistent with the most probable configuration in which pyridine molecules are adsorbed in an upright configuration with the N atom located at the Ti atom (Fig. 5c).^{63,64} In addition, as demonstrated in Fig. 4, locally enhanced fields would increase the transition probability of the dyes. Such an anisotropy should not appear from adsorption on the nanocrystals with random orientation. To verify this hypothesis, measurements were performed for DMASP-adsorbed TMC-800 with larger spaces between the nanocrystals (Fig. 2d); expectedly it was observed that there was no significant anisotropy (Fig. S15[†]). In some cases, the orientation of the DMASP tends to become more parallel to the long axis of TMC, as demonstrated in Fig. 6a,b. A similar situation has been observed for the DMASP molecules incorporated in a metal organic framework.⁶⁰ If the distance between two {001} facets decreases to ~ 1 nm, the DMASP would be more influenced by the crystal facet on the opposite side (Fig. 6c). Another possibility is that DMASP molecules are adsorbed on the {101} surfaces inside the pores. Such dyes might have the transition momenta along the long axis of TMC and be thus effectively coupled with the enhanced local fields (see Fig. 4b,d). These hypotheses are not supported by direct observation with TEM, but a much lower fluorescence intensity of the sample in Fig. 5a infers the smaller amount of adsorbed DMASP molecules, possibly due to the limited spaces. Based on these results, it is reasonable to conclude that the observed anisotropic adsorption of DMASP originates mainly from the nanospaces in

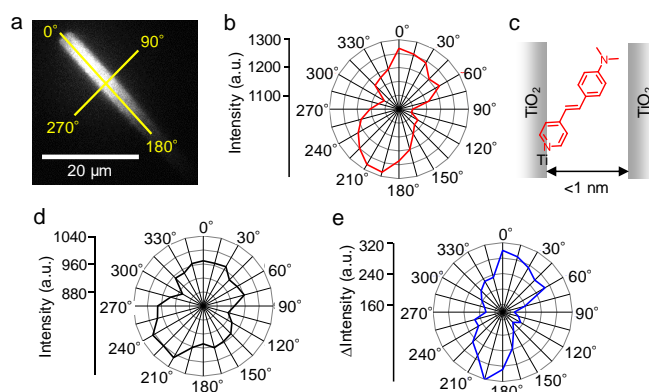


the mesocrystal structure.

Fig. 5 (a) A fluorescence image of DMASP-adsorbed TMC-400 observed under 405-nm laser irradiation. The long and short axes of TMC are defined as 0° and 90°, respectively. (b) Azimuthal plot of the fluorescence intensity response of the DMASP to the polarization of excitation light. (c) Illustration of the adsorbed DMASP in the oriented nanospace, based on the theoretical calculations for adsorption of pyridine on the TiO₂{001} surface.⁶³ The optimized structure of DMASP was obtained by density functional theory calculations at the B3LYP 6-31G(d,p) level using the Gaussian 09 package.⁶⁵

To clarify the involvement of the oriented nanospaces in photocatalysis, in situ observation of the photocatalytic reaction was combined with anisotropic evaluation. This approach allows us to test the status of preferential oxidation of the molecules in the oriented nanospaces. In the photocatalytic reaction, a 365-nm LED was used as an excitation light source and the LED power

was weakened by a neutral density (ND) filter to prevent photodegradation through direct excitation of DMASP. An interesting result evident in Fig. 6d,e is that the anisotropy became much weaker after UV irradiation for 30 min. As summarized in Table 1, the percentage difference ($= 100 \times \Delta I/I_{av}$) greatly decreased after UV irradiation, indicating that photodegradation of DMASP is promoted in the oriented nanospaces. The change in anisotropy is also seen in the azimuthal plot of the reduced components (Fig. 6e), which exhibits a profile with a strong anisotropy with respect to the profile before the UV irradiation (Fig. 6b). A similar tendency



was observed for other TMCs examined.

Fig. 6 (a) A fluorescence image of DMASP-adsorbed TMC-400. (b) Azimuthal plot of fluorescence intensities of DMASP-adsorbed TMC-400 as a response to the polarization of excitation light. (c) Illustration of the adsorbed DMASP in the oriented nanospace with < 1 nm width. (d) Azimuthal plot of fluorescence intensities of DMASP-adsorbed TMC-400 in panel b after UV irradiation ($6.6 \mu\text{W cm}^{-2}$). (e) Azimuthal plot of the reductions in fluorescence intensities upon UV irradiation.

It has been reported that the oxidation reaction of the adsorbates on TiO₂ is predominately initiated by direct hole transfer.⁶⁶ It is suggested that the pyridine and pyridine-containing compounds (e.g., benzo[b]pyridine) are predominantly oxidized by the photogenerated holes in TiO₂ to the radical cations centered on the pyridine ring.^{67,68} In addition, it has been verified that hydroxyl radical ($\cdot\text{OH}$) and singlet oxygen ($^1\text{O}_2$) are generated during the photocatalytic reactions and diffused away from the surface to air.⁶⁹⁻⁷² These airborne reactive oxygen species (ROS) would effectively oxidize the DMASP molecules in the nanospaces. In the oriented nanospaces, the DMASP molecules are closely sandwiched between two {001} facets, enhancing the efficiency of reactions with ROS. There are reports that the microporous structures of TiO₂ enhance the photocatalytic activity owing to scattering and reabsorption of UV light.^{73,74} The optical properties of the particle assembly having scales far below the wavelength of the excitation light are not only determined by these effects but also by the local electric fields associated with the structures. Therefore, it can be proposed that the oriented nanospaces by the specific facets provide a field more suitable for photocatalytic reaction than the surrounding environment.

Table 1 Fluorescence intensity changes of DMASP-adsorbed TMC-400 by UV irradiation

	I_{\max} (a.u.) ^a	I_{\min} (a.u.) ^a	ΔI (a.u.) ^b	$100 \times \Delta I/I_{\text{av}}$ (%) ^c
original	1284	1096	178	15.0
after photocatalysis	1010	908	102	10.6
difference	300	170	130	55.3

^a I_{\max} and I_{\min} are maximum and minimum fluorescence intensities, respectively, obtained from the azimuthal plot of the fluorescence intensities. ^b ΔI values were the fluorescence intensity differences, calculated from $I_{\max} - I_{\min}$. ^c The percentage differences were calculated from $100 \times \Delta I/I_{\text{av}}$, where the average fluorescence intensity (I_{av}) is calculated from $(I_{\max} + I_{\min})/2$.

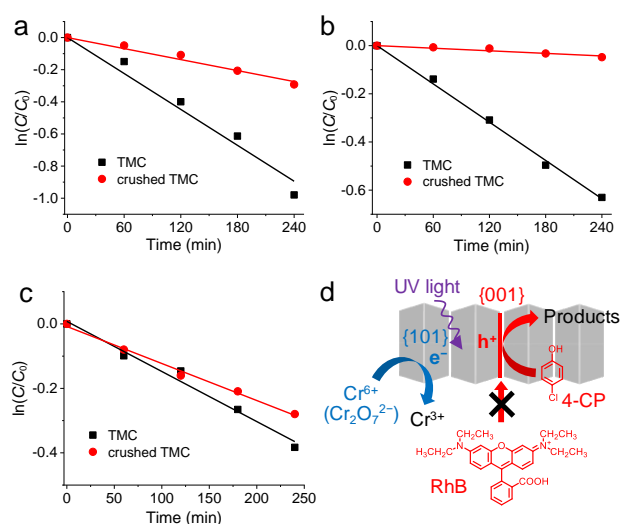
3.4 Selective photocatalytic reactions

To clarify the relationship between the mesocrystal structures and their photocatalytic performance, we examined the photocatalytic oxidation of RhB¹⁷ and 4-CP⁷⁵ and the photocatalytic reduction of Cr^{6+76} in aqueous phase as probe reactions. As shown in Fig. S15a-c†, the change in the absorbance spectra of RhB showed no significant shift in the peaks, suggesting that oxidative degradation mainly took place and the involvement of de-ethylation via direct excitation of RhB is excluded.⁷⁷ The absorbance changes of the characteristic peaks were monitored, and the relative activities of photocatalytic reactions were estimated (Fig. S16†). To verify superior properties of the superstructures, we compared the photocatalytic activities of TMCs with those of their crushed structures (Fig. S17†). The activity of the photocatalytic reaction was evaluated by irradiating a 365-nm LED (30 mWcm^{-2}) but without stirring to prevent the destruction of the mesocrystal structure during long-time reaction.

On the basis of a previous study,⁷⁸ the degradation rate of organics (k) can be described by a pseudo first-order kinetics with respect to the concentration (C) of the substrate in the bulk solution as given by the equation: $\ln(C_0/C) = kC$, where C_0 is the initial concentration in the bulk solution (Fig. 7a,b). To evaluate the selectivity in the photocatalytic reactions, a benchmark P25 TiO_2 , which consists of anatase and rutile crystalline phases, was also tested. As summarized in Table 2, the oxidative degradation rates of RhB and 4-CP of TMC were 1/112th and 1/29th that of P25, respectively, but the photoreduction reaction of Cr^{6+} was only half the value for P25. Because of the short penetration depth ($\sim 250 \text{ nm}$) of the 365 nm light⁷⁹ and its micrometer size, TMC is obviously disadvantageous in light absorption and light scattering compared with nanosized P25 (Table S1†). It is thus reasonable that the activity of the photocatalytic reaction becomes lower than P25 when the transport rate of the target molecule is lower than the rate of photocatalytic reaction under the present experimental conditions. However, a relatively high activity of photoreduction was observed despite a structural disadvantage of TMC, as shown in Table 2. This result can be explained by the fact that the $\{101\}$ facets, which act as reservoirs of photogenerated electrons, are exposed on the surface of TMC (Fig. 7d).

On the other hand, it is presumed that degradation reactions of RhB and 4-CP occurred effectively on the $\{001\}$ facets that contain many active five-coordinated Ti sites and accumulate the holes.^{17,33} For TMC, the reaction rate of RhB was 1.4 times that

of 4-CP, but it was 6.6 times for crushed TMC and 5.6 times for P25 (Table 2). Considering that the nanospaces formed by the $\{001\}$ facets have a size of $\sim 1.5 \text{ nm}$, it is difficult for RhB with a hydrodynamic diameter of 1.7 nm to access the $\{001\}$ facets of TMC (Fig. 6d).⁸⁰ This would be one of the reasons for the lower relative value (0.0089) of RhB than that (0.034) of 4-CP for TMC, as compared with P25. When the mesocrystal structure of TMC was destroyed by physical crushing (Fig. S16†), the degradation rate of RhB became comparable to that of 4-CP. This result suggests that the limited access of RhB to the interior surfaces of TMC has been resolved, again emphasizing the involvement of the oriented nanospaces by the $\{001\}$ facets. The amounts of adsorbed RhB molecules on pristine and crushed TMCs were determined as 0.34 and $0.22 \mu\text{mol g}^{-1}$, respectively. This 1.5-fold different can be reasonably explained by considering that the $\{001\}$ facets occupy $\sim 38\%$ of the total surface area (Fig. S4†). Additionally, the decrease in the activity of the crushed TMC is attributable to the suppression of efficient charge transport within the nanocrystal network in the



mesocrystals.¹⁸

Fig. 7 Kinetic linear fitting curves of (a) RhB and (b) 4-CP in neutral water, and (c) Cr^{6+} in H_2SO_4 aqueous solution at pH 3. (d) Illustration of selective photocatalytic redox reactions.

Table 2 Photocatalytic reaction rates and efficiencies

sample	oxidation rate, 10^{-5} s (relative value)		reduction efficiency, % ^a (relative value)
	RhB	4-CP	Cr^{6+}
TMC	6.2 (0.0089)	4.4 (0.034)	32 (0.39)
crushed TMC	1.9 (0.0027)	0.30 (0.0023)	24 (0.29)
P25	7.0×10^2 (1)	1.3×10^2 (1)	61 (1)

^a Obtained after UV irradiation for 4 h.

Conclusions

We newly synthesized rod-shaped TMCs with a unique structure in which TiO_2 nanocrystals expose the $\{101\}$ facets to the bulk solution and stack the $\{001\}$ facets forming oriented nanospaces

with a size of ~1.5 nm. From FDTD calculations, it was found that the nanospace exhibits the enhanced electric fields (maximum $EF > 4$), which should be useful for photocatalytic and photovoltaic applications.⁸¹ These nanospaces by the specific facets enable a certain regularity in the orientation of adsorbed dye molecules that efficiently degrade during photocatalytic reactions as compared with the ones adsorbed on the surrounding surfaces. Furthermore, it was suggested that the controlled nanospaces between the nanocrystals facilitate screening by molecular size and selective photocatalysis. As mentioned in the introduction section, there have been remarkable advances in the facet-engineering of photocatalytic materials besides TiO_2 in the recent years.⁸²⁻⁸⁴ Although the activity of present TMCs is not high enough for further photocatalytic applications because of their large size, the concept of oriented nanospace is versatile and thus expected to be a general strategy for tailoring efficient light energy conversion systems.

Conflicts of interest

There are no conflicts to declare.

Acknowledgements

This work was partially supported by JST PRESTO and JSPS KAKENHI Grant Numbers JP15H03771, JP18H01944, JP18H04517, and others.

Notes and references

- M. E. Davis, *Nature*, 2002, **417**, 813-821.
- A. Taguchi and F. Schueth, *Microporous Mesoporous Mater.*, 2004, **77**, 1-45.
- Y. Ren, Z. Ma and P. G. Bruce, *Chem. Soc. Rev.*, 2012, **41**, 4909-4927.
- H. Yamashita, K. Mori, Y. Kuwahara, T. Kamegawa, M. Wen, P. Verma and M. Che, *Chem. Soc. Rev.*, 2018, **47**, 8072-8096.
- C. Sanchez, L. Rozes, F. Ribot, C. Laberty-Robert, D. Grosso, C. Sassoie, C. Boissiere and L. Nicole, *C. R. Chim.*, 2010, **13**, 3-39.
- J. Gopalakrishnan, *Chem. Mater.*, 1995, **7**, 1265-1275.
- T. K. Kim, K. J. Lee, J. Y. Cheon, J. H. Lee, S. H. Joo and H. R. Moon, *J. Am. Chem. Soc.*, 2013, **135**, 8940-8946.
- Q.-L. Zhu and Q. Xu, *Chem. Soc. Rev.*, 2014, **43**, 5468-5512.
- M. A. Henderson, *Surf. Sci. Rep.*, 2011, **66**, 185-297.
- M. R. Hoffmann, S. T. Martin, W. Choi and D. W. Bahnemann, *Chem. Rev.*, 1995, **95**, 69-96.
- J. Schneider, M. Matsuoka, M. Takeuchi, J. Zhang, Y. Horiuchi, M. Anpo and D. W. Bahnemann, *Chem. Rev.*, 2014, **114**, 9919-9986.
- K. Nakata and A. Fujishima, *J. Photochem. Photobiol., C*, 2012, **13**, 169-189.
- Y. Nosaka and A. Y. Nosaka, *Chem. Rev.*, 2017, **117**, 11302-11336.
- A. Hagfeldt, G. Boschloo, L. Sun, L. Kloo and H. Pettersson, *Chem. Rev.*, 2010, **110**, 6595-6663.
- M. Zheng, H. Tang, L. Li, Q. Hu, L. Zhang, H. Xue and H. Pang, *Adv. Sci.*, 2018, **5**, 1700592.
- Z. Bian, T. Tachikawa and T. Majima, *J. Phys. Chem. Lett.*, 2012, **3**, 1422-1427.
- Z. Bian, T. Tachikawa, P. Zhang, M. Fujitsuka and T. Majima, *J. Am. Chem. Soc.*, 2014, **136**, 458-465.
- P. Zhang, T. Tachikawa, M. Fujitsuka and T. Majima, *Chem. Commun.*, 2015, **51**, 7187-7190.
- T. Tachikawa, P. Zhang, Z. Bian and T. Majima, *J. Mater. Chem. A*, 2014, **2**, 3381-3388.
- Z. Bian, T. Tachikawa, W. Kim, W. Choi and T. Majima, *J. Phys. Chem. C*, 2012, **116**, 25444-25453.
- P. Zhang, T. Ochi, M. Fujitsuka, Y. Kobori, T. Majima and T. Tachikawa, *Angew. Chem., Int. Ed.*, 2017, **56**, 5299-5303.
- T. Tachikawa and T. Majima, *NPG Asia Mater.*, 2014, **6**, e100.
- Z. Zhang, I. Karimata, H. Nagashima, S. Muto, K. Ohara, K. Sugimoto and T. Tachikawa, *Nat. Commun.*, 2019, **10**, Article Number: 4832.
- Z. Bian, T. Tachikawa, P. Zhang, M. Fujitsuka and T. Majima, *Nat. Commun.*, 2014, **5**, Article Number: 3038.
- M. A. Boles, M. Engel and D. V. Talapin, *Chem. Rev.*, 2016, **116**, 11220-11289.
- C. E. Rowland, I. Fedin, H. Zhang, S. K. Gray, A. O. Govorov, D. V. Talapin and R. D. Schaller, *Nat. Mater.*, 2015, **14**, 484-489.
- K. Whitham, J. Yang, B. H. Savitzky, L. F. Kourkoutis, F. Wise and T. Hanrath, *Nat. Mater.*, 2016, **15**, 557-563.
- G. Liu, J. C. Yu, G. Q. Lu and H.-M. Cheng, *Chem. Commun.*, 2011, **47**, 6763-6783.
- G. Liu, H. G. Yang, J. Pan, Y. Q. Yang, G. Q. Lu and H.-M. Cheng, *Chem. Rev.*, 2014, **114**, 9559-9612.
- S. Bai, L. Wang, Z. Li and Y. Xiong, *Adv. Sci.*, 2017, **4**, n/a.
- C. Guennemann, C. Haisch, M. Fleisch, J. Schneider, A. V. Emeline and D. W. Bahnemann, *ACS Catal.*, 2019, **9**, 1001-1012.
- T. Ohno, K. Sarukawa and M. Matsumura, *New J. Chem.*, 2002, **26**, 1167-1170.
- N. Murakami, Y. Kurihara, T. Tsubota and T. Ohno, *J. Phys. Chem. C*, 2009, **113**, 3062-3069.
- T. R. Gordon, M. Cargnello, T. Paik, F. Mangolini, R. T. Weber, P. Fornasiero and C. B. Murray, *J. Am. Chem. Soc.*, 2012, **134**, 6751-6761.
- P. Zhang, T. Tachikawa, Z. Bian and T. Majima, *Appl. Catal., B*, 2015, **176-177**, 678-686.
- M. D'Arienzo, J. Carbajo, A. Bahamonde, M. Crippa, S. Polizzi, R. Scotti, L. Wahba and F. Morazzoni, *J. Am. Chem. Soc.*, 2011, **133**, 17652-17661.
- T. Tachikawa, S. Yamashita and T. Majima, *J. Am. Chem. Soc.*, 2011, **133**, 7197-7204.
- J. Kou, C. Lu, J. Wang, Y. Chen, Z. Xu and R. S. Varma, *Chem. Rev.*, 2017, **117**, 1445-1514.
- Q. Wu and R. van de Krol, *J. Am. Chem. Soc.*, 2012, **134**, 9369-9375.
- L. Li, Z. Xu, F. Liu, Y. Shao, J. Wang, H. Wan and S. Zheng, *J. Photochem. Photobiol., A*, 2010, **212**, 113-121.
- H. Kominami, T. Nakaseko, Y. Shimada, A. Furusho, H. Inoue, S.-y. Murakami, Y. Kera and B. Ohtani, *Chem. Commun.*, 2005, DOI: 10.1039/b502909k, 2933-2935.
- T. Brezesinski, J. Wang, S. H. Tolbert and B. Dunn, *Nat. Mater.*, 2010, **9**, 146-151.
- K. Brezesinski, J. Wang, J. Haetge, C. Reitz, S. O. Steinmueller, S. H. Tolbert, B. M. Smarsly, B. Dunn and T. Brezesinski, *J. Am. Chem. Soc.*, 2010, **132**, 6982-6990.
- A. Agrawal, A. Singh, S. Yazdi, A. Singh, G. K. Ong, K. Bustillo, R. W. Johns, E. Ringe and D. J. Milliron, *Nano Lett.*, 2017, **17**, 2611-2620.
- D. Spagnoli, B. Gilbert, G. A. Waychunas and J. F. Banfield, *Geochim. Cosmochim. Acta*, 2009, **73**, 4023-4033.
- H. Zhang, J. J. De Yoreo and J. F. Banfield, *ACS Nano*, 2014, **8**, 6526-6530.
- J. J. De Yoreo, P. U. P. A. Gilbert, N. A. J. M. Sommerdijk, R. L. Penn, S. Whitelam, D. Joester, H. Zhang, J. D. Rimer, A.

- Navrotsky, J. F. Banfield, A. F. Wallace, F. M. Michel, F. C. Meldrum, H. Cölfen and P. M. Dove, *Science*, 2015, **349**, 498.
- 48 Y. Shiraishi, N. Saito and T. Hirai, *J. Am. Chem. Soc.*, 2005, **127**, 8304-8306.
- 49 Y. Shiraishi, D. Tsukamoto and T. Hirai, *Langmuir*, 2008, **24**, 12658-12663.
- 50 Y. Shiraishi, N. Saito and T. Hirai, *J. Am. Chem. Soc.*, 2005, **127**, 12820-12822.
- 51 H.-K. Lee and S.-W. Lee, *Chem. Lett.*, 2015, **44**, 604-606.
- 52 Z. Fang, L. Long, S. Hao, Y. Song, T. Qiang and B. Geng, *CrystEngComm*, 2014, **16**, 2061-2069.
- 53 P. Zhang, T. Tachikawa, M. Fujitsuka and T. Majima, *ChemSusChem*, 2016, **9**, 617-623.
- 54 H. Coelfen and M. Antonietti, *Angew. Chem., Int. Ed.*, 2005, **44**, 5576-5591.
- 55 H. G. Yang, C. H. Sun, S. Z. Qiao, J. Zou, G. Liu, S. C. Smith, H. M. Cheng and G. Q. Lu, *Nature*, 2008, **453**, 638-641.
- 56 M. Lazzeri, A. Vittadini and A. Selloni, *Phys. Rev. B Condens. Matter Mater. Phys.*, 2001, **63**, 155409/155401-155409/155409.
- 57 A. Taflove, S. C. Hagness and M. Piket-May, in *The Electrical Engineering Handbook*, ed. W.-K. Chen, Academic Press, Burlington, 2005, DOI: <https://doi.org/10.1016/B978-012170960-0/50046-3>, pp. 629-670.
- 58 K. Yoshihara, M. Sakamoto, H. Tamamitsu, M. Arakawa and K.-i. Saitow, *Adv. Opt. Mater.*, 2018, **6**, 1800462.
- 59 I. H. Öener, C. J. Querebillo, C. David, U. Gernert, C. Walter, M. Driess, S. Leimkuehler, K. H. Ly and I. M. Weidinger, *Angew. Chem., Int. Ed.*, 2018, **57**, 7225-7229.
- 60 P. Falcaro, K. Okada, T. Hara, K. Ikigaki, Y. Tokudome, A. W. Thornton, A. J. Hill, T. Williams, C. Doonan and M. Takahashi, *Nat. Mater.*, 2017, **16**, 342-348.
- 61 M. Sowmiya, A. K. Tiwari, Sonu and S. K. Saha, *J. Photochem. Photobiol., A*, 2011, **218**, 76-86.
- 62 K. Huang, J. Jia, X. Zhou, Y. Lin and X. Xiao, *J. Mater. Res.*, 2010, **25**, 32-38.
- 63 H. Kusama, H. Orita and H. Sugihara, *Langmuir*, 2008, **24**, 4411-4419.
- 64 I. X. Green, C. Buda, Z. Zhang, M. Neurock and J. T. Yates, Jr., *J. Phys. Chem. C*, 2010, **114**, 16649-16659.
- 65 M. J. Frisch, G. W. Trucks, H. B. Schlegel, G. E. Scuseria, M. A. Robb, J. R. Cheeseman, G. Scalmani, V. Barone, B. Mennucci, G. A. Petersson, H. Nakatsuji, M. Caricato, X. Li, H. P. Hratchian, A. F. Izmaylov, J. Bloino, G. Zheng, J. L. Sonnenberg, M. Hada, M. Ehara, K. Toyota, R. Fukuda, J. Hasegawa, M. Ishida, T. Nakajima, Y. Honda, O. Kitao, H. Nakai, T. Vreven, J. A. Montgomery, J. E. Peralta, F. Ogliaro, M. Bearpark, J. J. Heyd, E. Brothers, K. N. Kudin, V. N. Staroverov, R. Kobayashi, J. Normand, K. Raghavachari, A. Rendell, J. C. Burant, S. S. Iyengar, J. Tomasi, M. Cossi, N. Rega, J. M. Millam, M. Klene, J. E. Knox, J. B. Cross, V. Bakken, C. Adamo, J. Jaramillo, R. Gomperts, R. E. Stratmann, O. Yazyev, A. J. Austin, R. Cammi, C. Pomelli, J. W. Ochterski, R. L. Martin, K. Morokuma, V. G. Zakrzewski, G. A. Voth, P. Salvador, J. J. Dannenberg, S. Dapprich, A. D. Daniels, Farkas, J. B. Foresman, J. V. Ortiz, J. Cioslowski and D. J. Fox, *Journal*, 2009, DOI: citeulike-article-id:9096580.
- 66 T. Tachikawa, M. Fujitsuka and T. Majima, *J. Phys. Chem. C*, 2007, **111**, 5259-5275.
- 67 L. Cermenati, P. Pichat, C. Guillard and A. Albin, *J. Phys. Chem. B*, 1997, **101**, 2650-2658.
- 68 A. G. Agrios and P. Pichat, *J. Photochem. Photobiol., A*, 2006, **180**, 130-135.
- 69 K. Naito, T. Tachikawa, M. Fujitsuka and T. Majima, *J. Phys. Chem. B*, 2005, **109**, 23138-23140.
- 70 K. Naito, T. Tachikawa, S.-C. Cui, A. Sugimoto, M. Fujitsuka and T. Majima, *J. Am. Chem. Soc.*, 2006, **128**, 16430-16431.
- 71 K. Naito, T. Tachikawa, M. Fujitsuka and T. Majima, *J. Phys. Chem. C*, 2008, **112**, 1048-1059.
- 72 F. Yang, Y. Takahashi, N. Sakai and T. Tatsuma, *J. Phys. Chem. C*, 2011, **115**, 18270-18274.
- 73 J. H. Pan, X. Zhang, A. J. Du, D. D. Sun and J. O. Leckie, *J. Am. Chem. Soc.*, 2008, **130**, 11256-11257.
- 74 H. Li, Z. Bian, J. Zhu, D. Zhang, G. Li, Y. Huo, H. Li and Y. Lu, *J. Am. Chem. Soc.*, 2007, **129**, 8406-8407.
- 75 J. Theurich, M. Lindner and D. W. Bahnemann, *Langmuir*, 1996, **12**, 6368-6376.
- 76 I. Kretschmer, A. M. Senn, J. M. Meichtry, G. Custo, E. B. Halac, R. Dillert, D. W. Bahnemann and M. I. Litter, *Appl. Catal., B*, 2019, **242**, 218-226.
- 77 T. Wu, G. Liu, J. Zhao, H. Hidaka and N. Serpone, *J. Phys. Chem. B*, 1998, **102**, 5845-5851.
- 78 H. Al-Ekabi and N. Serpone, *J. Phys. Chem.*, 1988, **92**, 5726-5731.
- 79 S. Yamamoto, T. Sumita, Sugiharuto, A. Miyashita and H. Naramoto, *Thin Solid Films*, 2001, **401**, 88-93.
- 80 R. Holyst, A. Bielejewska, J. Szymanski, A. Wilk, A. Patkowski, J. Gapinski, A. Zywocki, T. Kalwarczyk, E. Kalwarczyk, M. Tabaka, N. Ziebach and S. A. Wieczorek, *Phys. Chem. Chem. Phys.*, 2009, **11**, 9025-9032.
- 81 Y. Bai, I. Mora-Sero, F. De Angelis, J. Bisquert and P. Wang, *Chem. Rev.*, 2014, **114**, 10095-10130.
- 82 R. Li, H. Han, F. Zhang, D. Wang and C. Li, *Energy Environ. Sci.*, 2014, **7**, 1369-1376.
- 83 W.-C. Huang, L.-M. Lyu, Y.-C. Yang and M. H. Huang, *J. Am. Chem. Soc.*, 2012, **134**, 1261-1267.
- 84 F. Chen, H. Huang, L. Ye, T. Zhang, Y. Zhang, X. Han and T. Ma, *Adv. Funct. Mater.*, 2018, **28**, 1804284.